

Article

Effects of Freeze-Thaw Cycles on Permeability Behavior and Desiccation Cracking of Dalian Red Clay in China Considering Saline Intrusion

Chen Chen ¹, Chaozhe Zhang ^{2,*},† , Xiao Liu ³, Xiaona Pan ⁴, Yenan Pan ³ and Pengjiao Jia ⁵ ¹ China Northeast Architectural Design & Research Institute Co., Ltd., Shenyang 110003, China² Institute of Geotechnical Engineering, School of Transportation, Southeast University, Nanjing 211189, China³ School of Civil Engineering, Shenyang Jianzhu University, Shenyang 110168, China⁴ China Construction Engineering Design & Research Institute Corporation Limited (Liaoning), Shenyang 110000, China⁵ School of Rail Transportation, Soochow University, Suzhou 215131, China

* Correspondence: chaozhe_zhang@163.com

† Current address: Institute of Geotechnical Engineering, School of Transportation, Southeast University, Nanjing 211189, China.

Abstract: Red clay with features of high liquid (plastic) limit, low permeability, medium-low compressibility and high strength is widely used in anti-seepage projects including roadbed, earth dam, tailings and landfill cover. This study investigates the hydraulic conductivity and propagation of desiccation cracks of compacted red clay in Dalian, China, considering the effect of freeze-thaw (F-T) cycles and saline intrusion. A series of compacted specimens were subjected to different F-T cycles at various controlled salt concentration of 0.2% and 4%. The surface cracking initiation and propagation process of compacted specimens under wetting-drying (W-D) cycles were monitored by Digital Image Correlation technique. The results indicated that permeability coefficient of compacted specimens increased significantly after the first F-T cycle regardless of specimens with variable dry density and salt concentration. The relationship between the number of F-D cycles and permeability coefficient can be expressed as the exponential function for Dalian red clay. Dry density and Saline inhibits the desiccation cracks of compacted specimens under W-D cycles. However, the F-T cycles have a modest promoting effect on crack propagation on the surface of saturated red clay. This study analyzes the underlying formation mechanisms of desiccation cracking-inducing geohazards and provides some guidance for the long-term performance of infrastructures upon saline intrusion and F-T cycles for red clay.

Keywords: red clay; freeze-thaw; wetting-drying; permeability behavior; desiccation cracking; digital image correlation



Citation: Chen, C.; Zhang, C.; Liu, X.; Pan, X.; Pan, Y.; Jia, P. Effects of Freeze-Thaw Cycles on Permeability Behavior and Desiccation Cracking of Dalian Red Clay in China Considering Saline Intrusion. *Sustainability* **2023**, *15*, 3858. <https://doi.org/10.3390/su15043858>

Academic Editor: Kaihui Li

Received: 3 January 2023

Revised: 13 February 2023

Accepted: 16 February 2023

Published: 20 February 2023



Copyright: © 2023 by the authors. Licensee MDPI, Basel, Switzerland. This article is an open access article distributed under the terms and conditions of the Creative Commons Attribution (CC BY) license (<https://creativecommons.org/licenses/by/4.0/>).

1. Introduction

Red clay with features of high liquid (plastic) limit, low permeability, medium-low compressibility and high strength is widely distributed in the tropical and subtropical regions including the south of China, and partially on the Qinghai-Tibet Plateau, as well as the northeastern coastal regions of China [1,2]. This high plasticity lateritic soil derived from carbonate rocks after long-term complex physical and chemical weathering is usually subjected to periodical freeze-thaw (F-T) cycles along with the destructive actions on infrastructure in seasonally frozen regions [3]. Cracking of the structure surface and excessive settlement upon spring thaw are the common damages caused by F-T cycles [4]. These damages associated with F-T cycling action are attributed to the numerous hydrophilic clay minerals [5]. The formation of ice crystals modifying the soil structure on the micro and macro-scale will weaken the strength and stiffness and increase the permeability of soils under F-T cycles [6–9]. Furthermore, the compacted clayed soils in geotechnical

engineering applications often come in contact with brine solution. The intrusion of saline from seawater poses severe influence on the hydro-mechanical properties of compacted clay in coastal areas, which alter the engineering behavior of soils owing to the interactions between clay particles and saline [10–13].

It is of great concern to investigate the effect of F-T cycles on the hydro-mechanical properties of clayed soils in frozen regions [14,15]. Regarding the variation of physical and mechanical properties, it is universally accepted that the void ratio of dense soils increases with F-T cycles and permeability coefficient always increases, without considering the volumetric changes. Regarding loose soils, the void ratio and strength obviously decline, which has been verified by many studies under experimental conditions [16–18]. The influencing factors of hydraulic conductivity include plasticity index [19], number of freeze-thaw cycles [20], initial hydraulic conductivity [21], temperature gradient and stress states [22]. The increase of permeability for clayed soils under freeze-thaw cycles is attributed to the occurrence of desiccation cracks and increasing pores.

Due to saline intrusion, an aggregated and densely stacked structure may be formed from the initial compacted structure of the clayed soil. This phenomenon is attributed to the suppression of the adsorption water film with the increase of the ion concentration, based on the electric double layer theory [23–27]. The effects of saline intrusion on clays' volumetric behaviors can be illustrated by two explanations: osmotic consolidation due to variation of electrostatic stresses between clay particles and osmotically-induced consolidation associated with the drainage of the pore fluid triggered by the osmotic pressure gradient [10,28]. However, research on the hydro-mechanical behaviors of red clay intruded by saline solutions is comparatively less reported in the literature.

The desiccation cracking behaviors of clayed soils have been studied under wetting-drying (W-D) cycles via laboratory tests, numerical simulation, digital image correlation method and field observation [29,30]. It is widely recognized that the desiccation cracks in the soil surface increase significantly in the first three W-D cycles and tend to be stable with increase in the number of W-D cycles [31]. The occurrence of desiccation cracks results in the increase of hydraulic conductivity, sometimes up to several orders of magnitude [32,33]. Li et al. (2011) [34] proposed that the propagation of desiccation cracks in clayed soil is comprised of the initial stage, the primary stage and the steady-state stage. Lu et al. (2016) [4] found that the geometrical morphology of the crack network slowly evolves from an irregularly rectilinear pattern towards a polygonal or quasi-hexagonal one for compacted clayed soil under freeze-thaw cycles. In general, Lakshmikantha et al. (2012) [35] indicated that the propagation of desiccation cracks can be restrained by means of decreasing the boundary condition, liquid limit and clay content or increasing soil strength and specimen thickness. Costa et al. (2018) [36] developed a theoretical solution to predict the spacing-to-depth ratio of parallel desiccation cracks in long desiccating soil layers based on stress relief and energy balance methods. Pouya et al. (2019) [37] proposed an energy approach to investigate soil desiccation cracking as a complement to the stress approach. It is noted that the simple model with limited parameters fails to characterize the desiccation cracking process precisely due to the complexity of soils [38,39].

The aforementioned studies revealed the separate effects of several climatic variables (e.g., freeze-thaw cycles, wetting-drying and saline intrusion) on the clayed soil. However, less attention has been paid to the permeability of clayed soil upon saline intrusion and freeze-thaw cycles, especially for red clay. Meanwhile, the soil cracking process of red clay under varying freeze-thaw cycles and wetting-drying cycles remains poorly understood. For this reason, in this paper, a series of freeze-thaw and wetting-drying tests for Dalin red clay in China were conducted to investigate the permeability behaviors and desiccation cracking of compacted red clay taking into account saline intrusion at different dry densities. By means of a Digital Image Correlation (DIC) technique, the evolution of desiccation cracks induced by W-D cycles was monitored in relation to soil evaporation activities.

2. Materials and Methods

2.1. Materials

The soil tested in this study was collected from a subgrade site located in Dalian Jinzhouwan International Airport, Liaoning Province, China, and was a type of red clay, which typically exhibits poor engineering performance particularly when saturated, after marine corrosion and under freeze-thaw conditions. The mechanical and physical properties of red clay as per ASTM D2487-11 (2011) [40] are listed in Table 1. The Atterberg limits were tested by the fall cone method. The grain size characteristic of red clay was measured by sieving and densimeter methods, and is shown in Figure 1. The specific gravity values of red clay were obtained according to ASTM D854-10 (2010) [41]. Sodium chloride (NaCl) with 99% content and relative molecular weight of 58.44 was used to consider marine corrosion of red clay.

Table 1. Mechanical and physical properties of red clay.

Property	Values
Unit weight, γ (kN/m ³)	16.0
Specific gravity, G_s	2.72
Initial water content, (%)	15.5
Liquid limit, w_L (%)	39.73
Plastic limit, w_P (%)	22.3
Optimum water content, (%)	19.7
Grain size distribution (%)	-
Clay (<0.005 mm)	1.6
Silt (0.005–0.075 mm)	39.8
Sand (>0.075 mm)	58.6
Uniformity coefficient, C_u	4.3
Maximum dry density, ρ_d (g/cm ³)	1.55

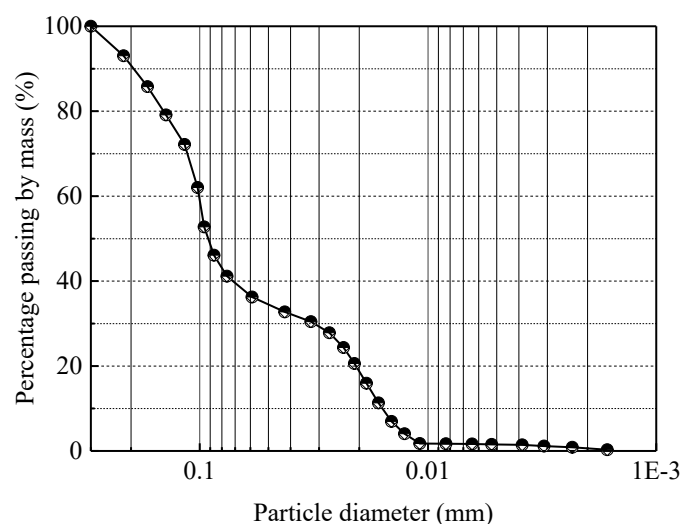


Figure 1. Gradation curve of red clay.

2.2. Specimen Preparation

Several steps for preparing specimens were conducted as shown in Figure 2. Two batches of specimens were compacted: (i) 36 disc specimens with diameter of 61.8 mm and height of 40 mm for measuring permeability coefficient and (ii) 9 disc specimens with diameter of 61.8 mm and height of 20 mm for observing the cracking characteristic. Three influencing factors were considered: dry density (ρ_d), salt concentration (T_{salt}) and number of freeze-thaw cycles ($N_{\text{F-T}}$). Since dry density affects the permeability and cracking development of red clay, ρ_d of 1.35 g/cm³, 1.45 g/cm³ and 1.55 g/cm³ are adopted based on natural dry density of 1.385 g/cm³. Since the average salt concentration in seawater

is generally 3.5%, the salt concentration in seawater closer to the coastline is affected by freshwater from land, resulting in T_{salt} of 1.2% during the dry season in winter and T_{salt} of 0.25% during the summer flood season. Therefore, the adopted T_{salt} in this study are 0, 2% and 4%. The soil was mixed with saline water to prepare the specimens with designed T_{salt} . Subsequently, the specimens were saturated by pumping in the saturated saline solution with the same salt concentration as the compacted specimens. The upper and lower surfaces of the specimens were padded with a filter paper slightly larger than the area of the ring knife to prevent the loss of soil particles. The permeable stones were placed on both surfaces of the specimens and fixed on the saturator. Then the specimen saturator was placed in a waterless autoclave for pumping saturation. After pumping close to atmospheric pressure and continuing for 1 h, saline solution was slowly injected into the autoclave. A stable vacuum was maintained in the autoclave until the saline solution completely submerged in the saturator. Subsequently, the autoclave vacuum was discharged to keep the specimens under saline solution for 12 h. However, it is a pity that the water content and degree of saturation at the saturated state of the specimen was not observed during the tests. Considering the influence of number of F-T cycles on permeability coefficient before the occurrence of the desiccation cracks, $N_{\text{F-T}}$ of 0, 1, 2 and 4 for compacted specimens are adopted in permeability tests. Consequently, 36 groups of tests were conducted taking account of the aforementioned three influencing factors. To effectively reduce the number of tests, the orthogonal experiment method was used to optimize the test scheme for desiccation cracks observation, as shown in Table 2. Label "RC-A-B-C" indicates a red clay compacted specimen with dry density of A and salt concentration of B subjected to C cycle(s) of freeze-thaw.

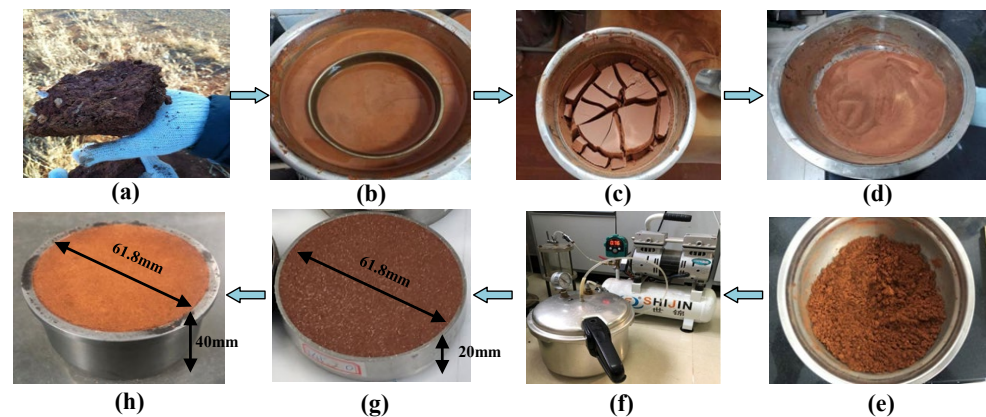


Figure 2. Procedures of the specimen preparation; (a) soil sample in field; (b) sieve and soaking; (c) drying soil sample; (d) grinding soil sample; (e) mixed soil sample; (f) soil sample saturation; (g) specimens for cracking tests; (h) specimens for permeability tests.

Table 2. Scheme of W-D cycle tests.

Specimen Number	Dry Density, ρ_d (g/cm^3)	Salt Concentration, T_{salt} (%)	Number of Freeze-Thaw Cycles, $N_{\text{F-T}}$
RC-1.35-0-0	1.35	0	0
RC-1.35-1-2	1.35	2	1
RC-1.35-2-4	1.35	4	2
RC-1.45-1-0	1.45	0	1
RC-1.45-0-2	1.45	2	0
RC-1.45-4-4	1.45	4	4
RC-1.55-2-0	1.55	0	2
RC-1.55-4-2	1.55	2	4
RC-1.55-0-4	1.55	4	0

2.3. Testing Procedures

2.3.1. Freeze-Thaw Cycles

Two types of specimens subjected to F-T cycles were carried out according to the F-T cycling specification stipulated in ASTM D560/D560M-16 (2016) [42]. A complete F-T cycle consists of freezing the specimens for 12 h and thawing the specimens for another 12 h. The closed-system F-T cycles during which specimens' water content remains constant are employed considering the low permeability of compacted red clay. The temperature applied in these tests varied from -10°C to 24°C , referring to the local climate records in Dalian. The specimens wrapped in preservative film were placed in the Constant Temperature and Humidity Chamber (CTHC) at a precision of 0.01°C for 12 h of freezing (see Figure 3a). The adopted time of freezing, 12 h, is considered sufficient to achieve equilibrium in temperature [3]. Subsequently, compacted specimens were removed from the CTHC and put into the standard curing chamber for 12 h thawing. This F-T procedure is repeated to reach the designated number of F-T cycles.

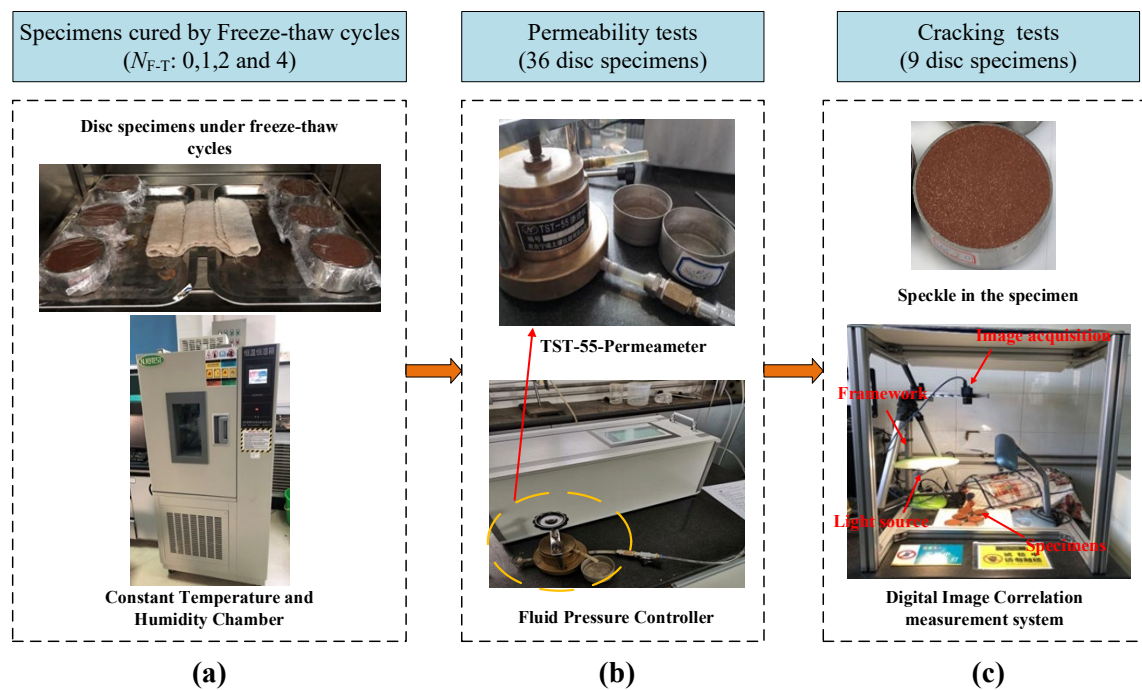


Figure 3. Procedures and tools used for laboratory tests; (a) specimens cured by Freeze-thaw cycles; (b) permeability tests; (c) cracking tests.

2.3.2. Wetting-Drying Cycles

The W-D cycle process was used to simulate the effect of rainfall on the shrinkage and cracking of the red clay. In this study, six W-D cycles were applied to the specimens after photographic analysis for ten days; then 20 g of distilled water was sprayed on the surface of the specimen, and the time of the first image capture was recorded after spraying [43,44]. After an interval of 24 h, the spraying operation was repeated and the specimens were exposed to room conditions to make water evaporate until starting the next cycle.

2.3.3. Permeability Measurement

As shown in Figure 3b, the TST-555 Permeameter was used to measure the permeability behavior of red clay specimens subjected to F-T cycles. Stable fluid pressure varying from -80 kPa to 1000 kPa was provided by the Fluid Pressure Controller. The specimens after F-T cycles were loaded into the Permeameter below the filter paper, permeable stone and sealing gasket soaked with distilled water, according to the permeability testing specifications stipulated in GB/T 50123-2019 [45]. Considering the water evaporation during

the permeability tests, two dry containers were placed under the same conditions, and a certain amount of water was poured into the container before the permeability tests. The water evaporation in the container was regarded as the evaporation compensation value of seepage during permeability tests. Since red clay has a small permeability coefficient and large seepage damping coefficient, a large seepage force will cause the soil structural damage and large deviations in the test results [46]. Therefore, a constant head of 30 kPa was adopted for the tests.

2.3.4. DIC Technology

The basic principle of DIC technology is to analyze the variation of several speckled patterns between reference and current images [47]. The field of displacement and corresponding strains of two images can be obtained by comparing the grayscale distributions in the corresponding pixel patterns [48,49]. As shown in Figure 3c, a photographic system was installed, including three parts: framework, image acquisition and light source. To ensure that each image was taken from the same direction and distance, the camera was fixed using fasteners. Two table lamps were prepared to provide stable light source. White kaolin composed of particle with a diameter of about 5 μ m was used as a speckle pattern on the top surfaces of 9 disc specimens. Approximately 10 g of white kaolin was evenly placed in a 0.15 mm sieve. The white kaolin was evenly spread on the specimen surface from a certain height by manually vibrating the sieve to form the required scattered spots for the tests.

Each saturated specimen was photographed for a total of 16 days. The surface shrinkage of the saturated specimen was observed for the first 10 days of photography. Subsequently, compacted specimens were subjected to W-D cycles from the 11th day. The spraying method was used to spray 20 g of quantitative distilled water on the specimen surface and the time of the first image capture after the spraying was recorded. The spraying operation was repeated after an interval of 24 h. The water evaporated naturally in a conventional room environment during this period. A total of 6 W-D cycles were performed repeatedly to simulate the effect of rainfall on desiccation cracking of the red clay surface. These obtained images were analyzed by 2D-DIC software-GOM Correlate 2016. The images were imported to the software and the whole specimen surface was regarded as the calculation scale, which meant that the diameter of the specimen (61.8 mm) was set as the point distance to reflect the actual size. Subsequently, the surface component was created with facet size of 30 pixels.

3. Results and Analyses

3.1. Permeability Characteristic

In order to reduce the influence of initial water content, the saturated specimens were adopted to investigate permeability characteristics under closed condition. Figure 4 presents the variation curves of permeability coefficient with F-T cycles under constant ρ_d . It can be observed that permeability coefficient of specimens increases with N_{F-T} under the constant ρ_d . In particular, the permeability coefficient increases significantly with the growth of 5.52×10^{-5} cm/s after the first F-T cycle, and then increases slightly. During the freezing process, there will be a temperature gradient from the surface to the center of the specimens. The unfrozen liquid water and dissolved salt distributed in the center of the specimens will diffuse and migrate to the soil's surface. The emerging ice and salt crystals on the surface of specimens cause the expansion of the soil volume and alter the pore morphology of the soil structure. The large pores gradually increase due to the transformation of small and medium-size pores. Conversely, because of the higher surface temperature of the specimens than that of the center, the melting of ice crystals on their surface, accompanied by NaCl dissolved in free water, migrate toward the center of the specimen.

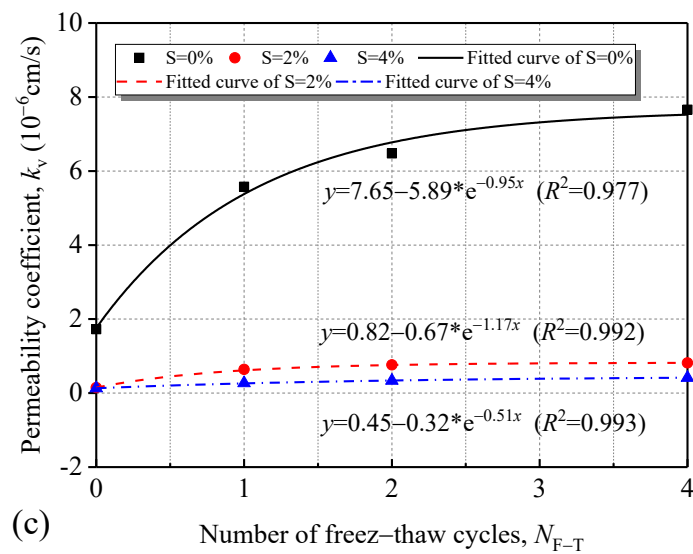
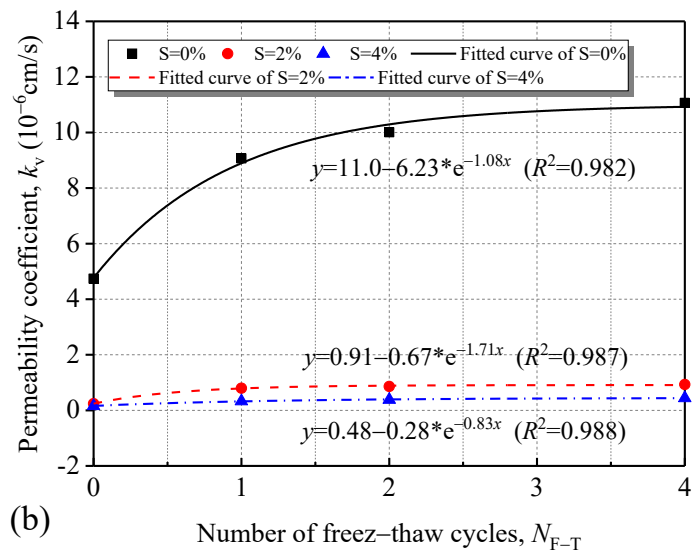
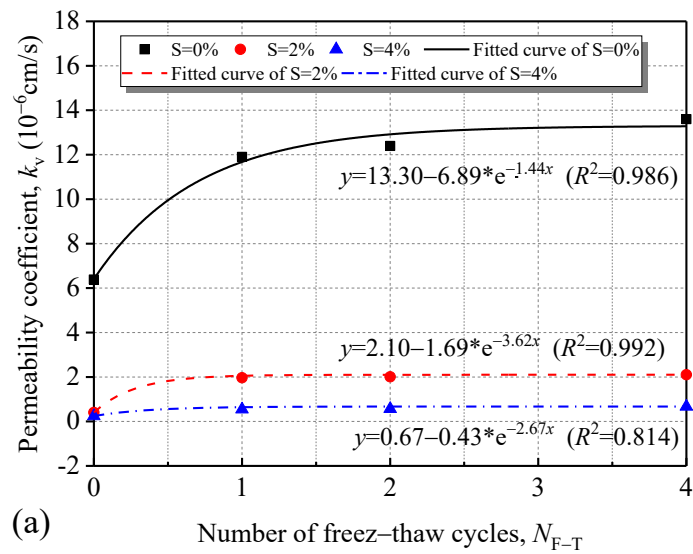


Figure 4. Variation curves of permeability coefficient with F-T cycles under constant ρ_d ; (a) ρ_d of 1.35 g/cm^3 ; (b) ρ_d of 1.45 g/cm^3 ; (c) ρ_d of 1.55 g/cm^3 .

With the increase of N_{F-T} , the inflation force will be applied to the pores in compacted specimens due to the repeated migration of pore water and saline. A large number of pores and micro-cracks will appear, and finally channels for water migration emerge in the specimens, resulting in their increasing permeability coefficient [50,51]. It should be noted that the permeability coefficient of compacted specimens increases significantly after the first F-T cycle regardless of specimens with variable T_{salt} and ρ_d . The reason is that migration channels have formed by seepage back and forth in the soil structure. The permeability coefficient increases along with the increase of N_{F-T} , with an obviously decreasing growth compared to N_{F-T} of 1.

In addition, the exponential function can be used to fit the quantitative relationship between the number of F-D cycles and the permeability coefficient. The results indicate that the permeability coefficient of saturated specimens increases exponentially with the number of F-T cycles and permeability coefficient of compacted specimens without saline intrusion can improve twice as much as that of specimens without F-T cycling action. Basically, R^2 of all fitted curves is greater than 95%, which proves that exponential function can be used to predict the permeability coefficient of red clay subjected to F-T cycles.

Figure 5 shows the variation curves of permeability coefficient with F-T cycles under constant T_{salt} . It can be seen from Figure 5 that the permeability coefficient of specimens presents an overall increasing trend with the increase of N_{F-T} . However, the permeability coefficient of specimens with constant T_{salt} decreases with the increase of ρ_d . The greater the dry density, the greater the weight of the specimen under the constant volume of the cutting ring, so the specimen is in a denser state where soil particles are closely connected with fewer pores. Due to fewer pores in specimens, the ability of the pore water migration is weakened under F-D cycles, leading to difficulty in forming channels for pore water and decrease of the permeability coefficient.

It is worth noting that the permeability coefficient of specimens with T_{salt} of 2% and ρ_d of 1.35 g/cm³ increases significantly after the first F-T cycle. Regarding the specimens with small dry density, the quantity and size of pores in the soil are large. Besides, T_{salt} of 2% can be completely dissolved in the pore water of the soil. During the period of freezing, pore water freezes into ice and some sodium chloride crystals are precipitated out due to the reduced pore water. Ice and sodium chloride crystals promote the change of soil structure and rearrangement of soil particles to make larger pores in the soil [52]. The increase in permeability coefficient of specimens is attributed to the original pores and the larger pores produced during soil freezing. Furthermore, the permeability coefficient of compacted specimens decreases with the increase of T_{salt} under the constant ρ_d . The reason is that the high content of sodium chloride cannot dissolve in pore water thoroughly, and partial sodium chloride in the form of crystal is precipitated and distributed in the soil pores, which is not conducive to the formation of migration channels.

3.2. Desiccation Cracking

3.2.1. Crack Observation

Figure 6 presents the evolution of desiccation cracks on the surface of specimens where T is the day of the image collection and $T = 1$ is the day of the initial image. The shrinkage rates of specimens can be reflected by the separation time between cutting rings and specimens. The separation time for specimens with T_{salt} of 0.2% and 4% are 1 day, 2 days and 3 days, respectively. This indicates that the evaporation rate of water on the surface of specimens decreases as T_{salt} of specimens increases. However, dry density and the number of F-T cycles have a limited effect on the dry shrinkage of specimens.

In addition, the length and width of desiccation cracks on the surface of specimens increase with the increase of N_{F-T} . The development of cracks is mainly due to the evaporation of pore water in specimens. Soil particles are compacted due to the matric suction resulting from water's evaporation, which increases the tensile stresses between soil particles [52,53]. The distribution of tensile stress is not uniform because of the inhomogeneity of the soil particles. Shrinkage cracks occur when the tensile stress exceeds the matric

suction of soil particles. Once cracks appear on the surface of the soil specimens and the rate of water evaporation increases owing to the formation of cracks. In the area where the cracks have appeared, the cracks expand rapidly and intersect with each other continuously to form the crack grid. As the water evaporates, the cracks start to bifurcate and derive more branching cracks, and the divided block area on the surface of specimens tends to stabilize until there are no more branching cracks.

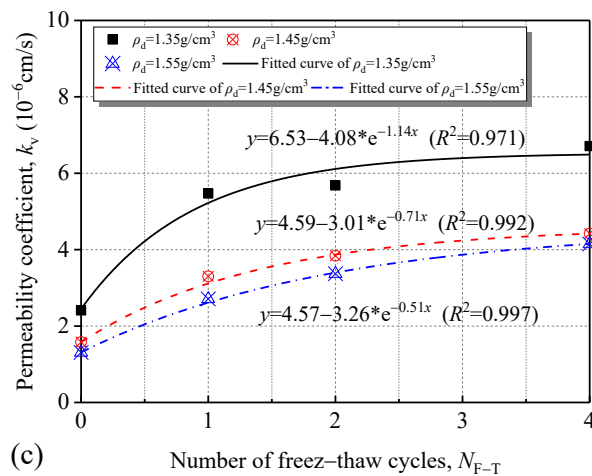
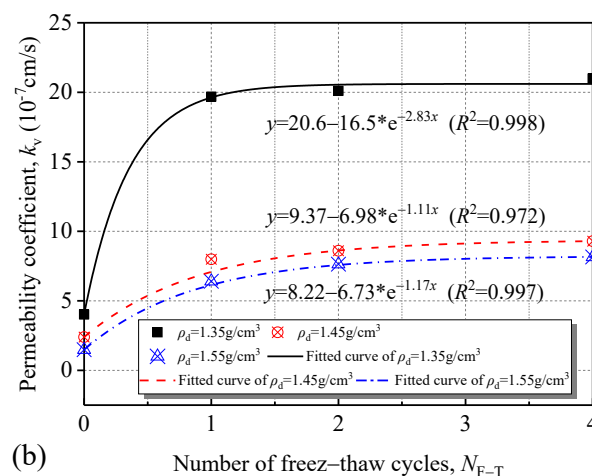
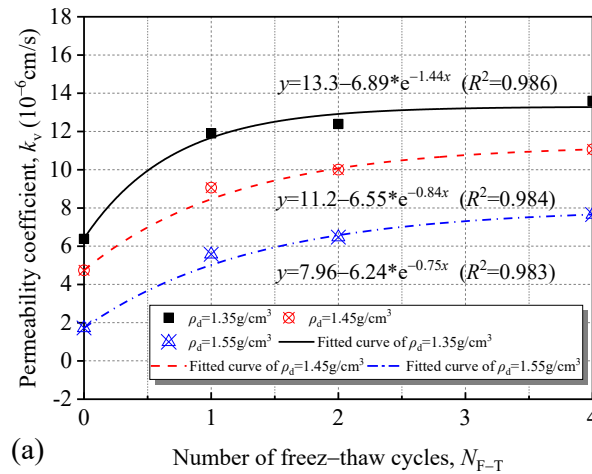


Figure 5. Variation curves of permeability coefficient with F-T cycles under constant T_{salt} : (a) T_{salt} of 0; (b) T_{salt} of 2%; (c) T_{salt} of 4%.



Figure 6. Cont.



Figure 6. Cont.

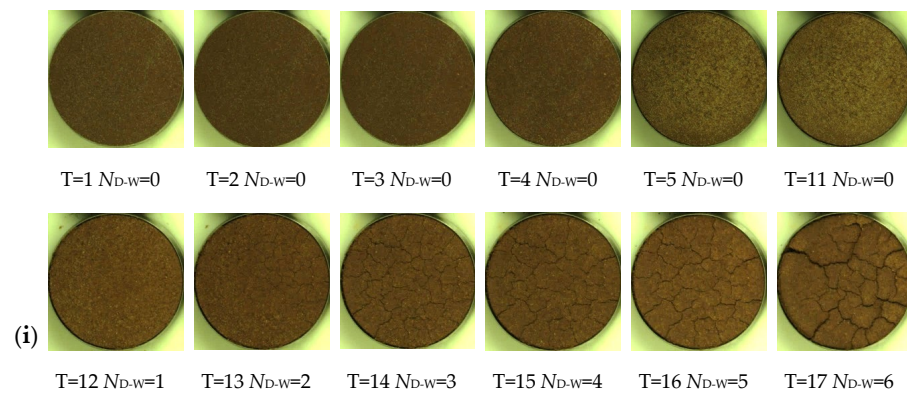


Figure 6. Diagrams of desiccation cracks; (a) RC-1.35-0-0; (b) RC-1.35-2-1; (c) RC-1.35-4-2; (d) RC-1.45-0-1; (e) RC-1.45-2-0; (f) RC-1.45-4-4; (g) RC-1.55-0-2; (h) RC-1.55-2-4; (i) RC-1.55-4-0.

The first W-D cycle was conducted after the occurrence of cracks. Since the water enters the cracks, the increasing free water in the pores of specimens weakens the constraint effect of the matrix suction on the water molecules. Due to the shrinkage cracks of specimens, the larger contact area between the water molecules and the air accelerates the water evaporation. So the existing cracks on the surface of specimens become wider and longer. After the second W-D cycle, the width and length of the original cracks are further widened and lengthened. Subsequently, the cracks tend to be stable with the increase in W-D cycles. In general, the length and width of cracks increase greatly in the first and second W-D cycles, and stabilize after N_{D-W} of 6, as shown in Figure 7.

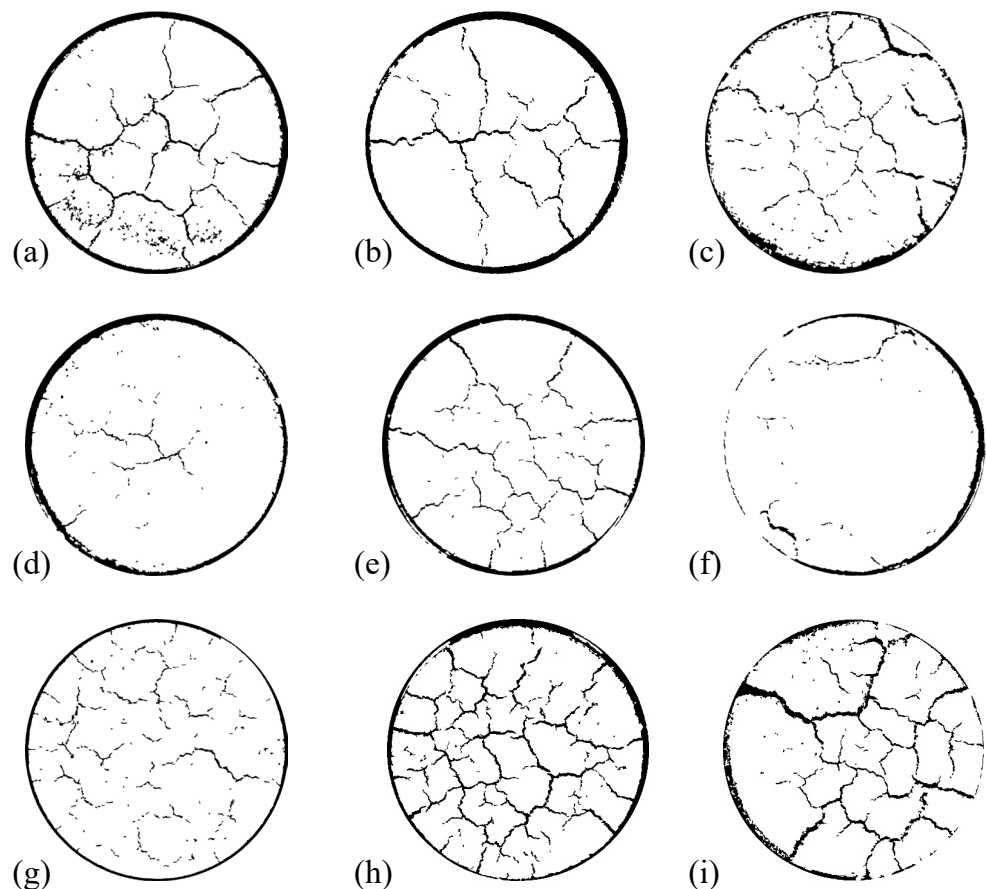


Figure 7. Binary results of desiccation cracking; (a) RC-1.35-0-0; (b) RC-1.35-2-1; (c) RC-1.35-4-2; (d) RC-1.45-0-1; (e) RC-1.45-2-0; (f) RC-1.45-4-4; (g) RC-1.55-0-2; (h) RC-1.55-2-4; (i) RC-1.55-4-0.

3.2.2. Effect of Dry Density on Cracks of Saturated Red Clay

The deformation behaviors of compacted specimens are analyzed by the strains of the selected random points on the surface of specimens in the direction of X at different times. The settings of the coordinate axes are shown in Figure 8. In following analysis, the strain direction is not considered, but only the amount of strain change.

Figure 9 presents variation curves of radial strain with time on the surface of RC-1.35-0-0. It can be seen from Figure 9 that the variation values of radial strain vary uniformly with a maximum value of 17.63% as the time within ten days increases. The variation range of strain value is from -20% to 20%. The radial strain of the specimen subjected to the first W-D cycle increases significantly with a maximum value of 34.01%. The maximum increment of the radial strain is 20.54% after the second W-D cycle. Subsequently, the increase of radial strain tends to level off in the following cycles.

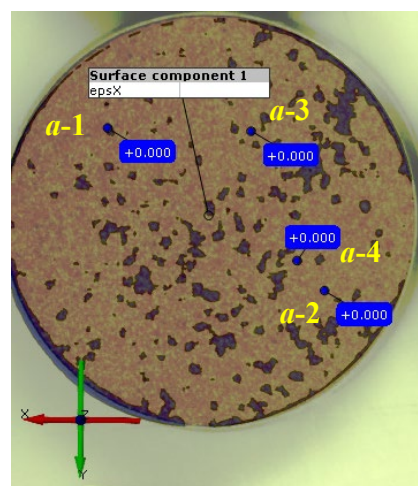


Figure 8. Coordinate axis diagram.

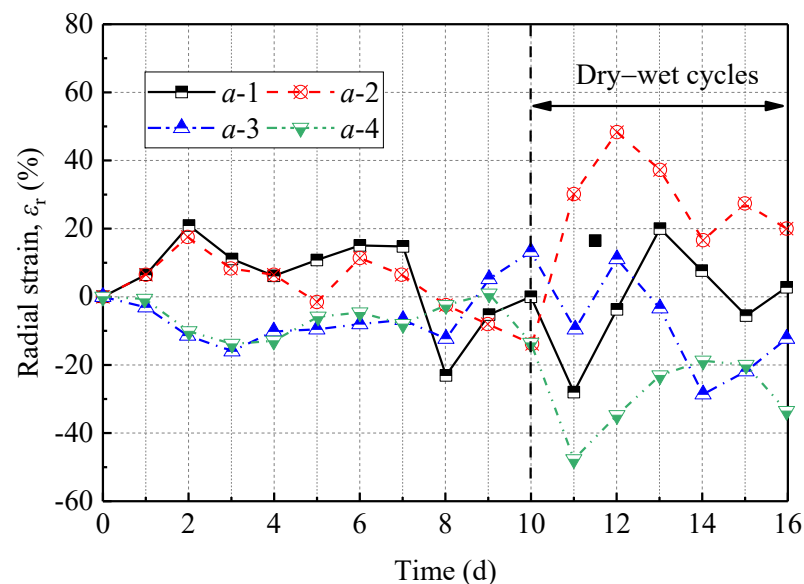


Figure 9. Variation curves of radial strain with time on RC-1.35-0-0 surface.

The variation curves of radial strain with time on the surface of RC-1.45-0-1 are shown in Figure 10. The trend of the radial strain variation throughout the drying shrinkage process was similar to that of the RC-1.35-0-0, but the strain varied from 5% to 10%. Besides, the radial strain of the specimen rises obviously with a maximum value of 9.30% after the

2nd and 3rd drying shrinkage. In the W-D cycle test, the evolution trend of the radial strain is the same as that of RC-1.35-0-0, where the variation of radial strain is more considerable, with a maximum value of 11.53% after the 1st and 2nd W-D cycles.

As for RC-1.55-0-2, the overall development pattern of radial strain is similar to that of RC-1.35-0-0 and RC-1.45-0-1, but the strain variation fluctuated in the range of 2% to 10% (see Figure 11), which was smaller than that of the aforementioned two specimens. The radial strain on the surface of specimens both varied significantly in the first two days of the dry shrinkage and W-D cycles tests, with maximum values of 8.17% and 8.04%, respectively. This illustrated that the variation values of the radial strain decreases with the increase of ρ_d . The number of desiccation cracks on the RC-1.45-0-1 surface is significantly more than that on RC-1.35-0-0 and RC-1.55-0-2 surfaces, indicating that the cracks propagation of specimens was inhibited with the increase of ρ_d , as shown in Figures 12–14.

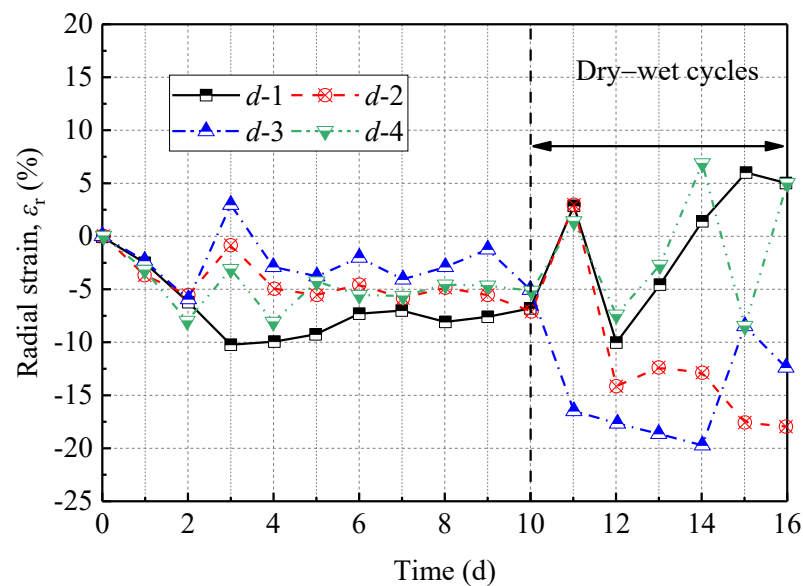


Figure 10. Variation curves of radial strain with time on RC-1.45-0-1 surface.

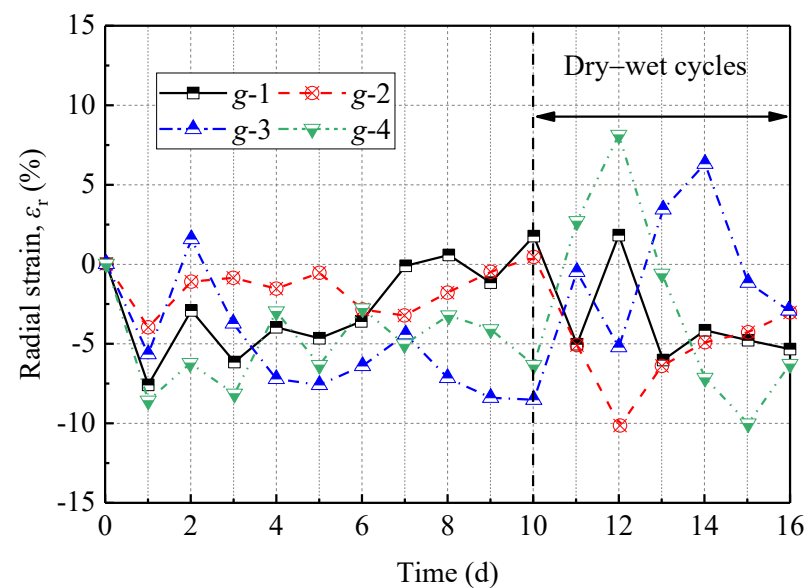


Figure 11. Variation curves of radial strain with time on RC-1.55-0-2 surface.

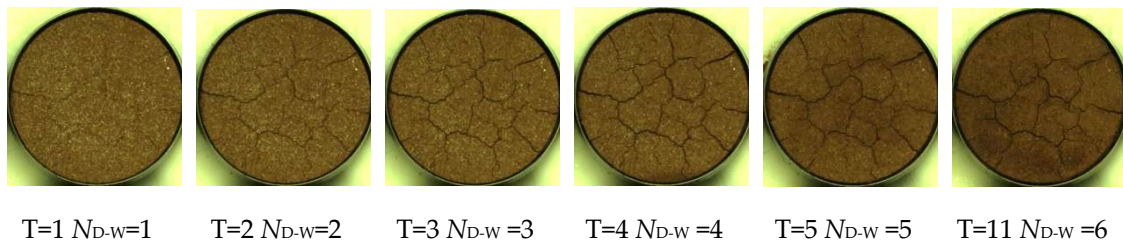


Figure 12. The crack propagation of RC-1.35-0-0 under W-D cycles.

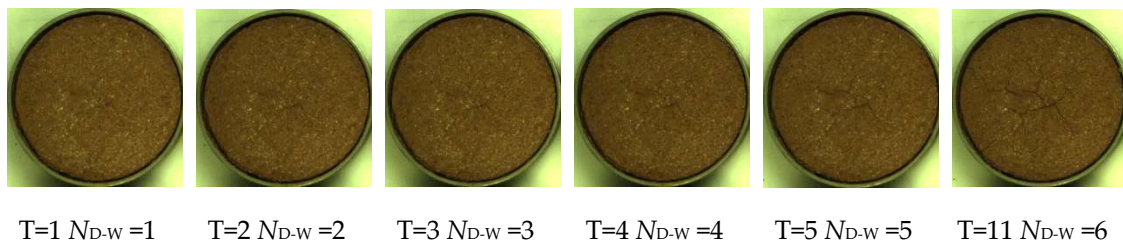


Figure 13. The crack propagation of RC-1.45-0-1 under W-D cycles.

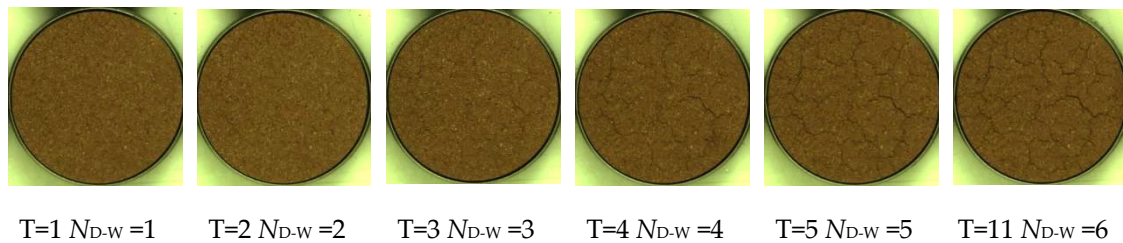


Figure 14. The crack propagation of RC-1.55-0-2 under W-D cycles.

The free water in the pores of specimens reduces due to the water evaporation. A type of curved liquid surface is formed between the free water surface and the soil particles and the surface tension of the curved liquid surface has a reordering effect on the soil particles. Regarding specimens with large dry density, the cohesive strength between the soil particles is relatively large. The matrix suction attributed to the reduction of free water fails to exceed the cohesive strength between the soil particles. Therefore, the unbroken connection between soil particles reflects the slight variation of radial strain at the macroscopic level [50,54]. Meanwhile, the decreasing pores in specimens lead to the increasing resistance of water molecules migrating from the interior of specimens to their surfaces. The rate of water evaporation will decrease as the dry density increases, which is the main reason for crack propagation in compacted specimens under unloaded conditions. Therefore, the increase of dry density has a certain inhibitory effect on the desiccation cracking of specimens under W-D cycles.

It can be seen from Figures 9–11 that radial strain of RC-1.35-0-0 with k_v of 6.381×10^{-6} cm/s is much larger than those of RC-1.45-0-1 with k_v of 9.065×10^{-6} cm/s and RC-1.55-0-2 with k_v of 6.476×10^{-6} cm/s. This indicates that dry density has the more apparent influence on the desiccation cracking than salt concentration and F-T cycle to some extent for red clay.

3.2.3. Effect of Freeze-Thaw Cycles on Cracks of Saturated Red Clay

The maximum variation values of radial strains of RC-1.35-0-0, RC-1.45-0-1 and RC-1.55-0-2 are 34.01%, 11.53%, and 8.04%, respectively, indicating that the maximum variation strain decreased with the increase of N_{F-T} . Although the aforementioned specimens possess similar permeability coefficients, the maximum variation values of radial strains have

great differences. In conclusion, F-T cycles have less effect on the cracking propagation than dry density of specimens. Meanwhile, it was observed that the separation time between the edge and the cutting ring of RC-1.35-0-0 (first day) is later than that of RC-1.45-0-1 and RC-1.55-0-2 (second day), which contradicts the conclusion that the number of desiccation cracks on the surfaces of compacted specimens decreases with ρ_d . This phenomenon is because the F-T cycles promote water migration to form migration channels in specimens. The larger pores are beneficial in improving the evaporation of pore water for red clay compacted specimens. The increasing air entering specimens through a large number of pores can increase the matric suction between soil particles, resulting in the soil particles being redistributed to enlarge desiccation cracks when the matric suction exceeds the cohesive strength between soil particles. In summary, the F-T cycles have a modest promoting effect on crack propagation on the surface of saturated red clay.

3.2.4. Effect of Salt Concentration on Cracks of Saturated Red Clay

Figure 15 illustrates variation curves of radial strain with time on the surface of RC-1.35-2-1. It can be seen from Figure 15 that the changes of radial strain on the soil surface vary uniformly with the increase of tested days within 10 days, with a fluctuation range from 5% to -10%. The variation value of radial strain of the specimen was higher on the 2nd and 3rd days of the test, with a maximum value of 12.66%. Subsequently, the radial strain of this specimen increased significantly after the first two W-D cycles, with maximum variation values of 18.13% and 14.28%, respectively. The increase of radial strain varies uniformly during 3rd to 6th W-D cycles. Compared to RC-1.35-2-1, radial strain values of RC-1.35-4-2 fluctuate more significantly with a range from 10% to 15% during the dry shrinkage process, as shown in Figure 16.

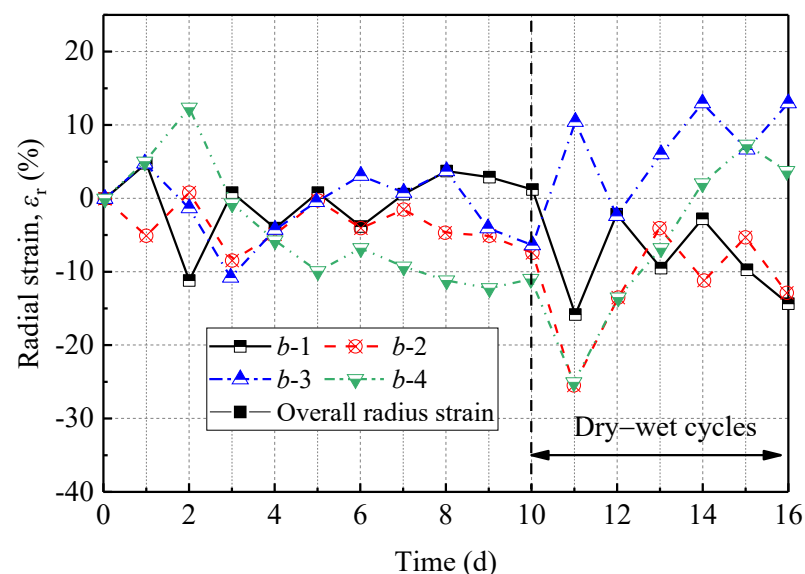


Figure 15. Variation curves of radial strain with time on RC-1.35-2-1 surface.

Figures 9, 15 and 16 state that the maximum increment of radial strain for RC-1.35-0-0 with k_v of 6.381×10^{-6} cm/s, RC-1.35-2-1 with k_v of 1.968×10^{-6} cm/s and RC-1.35-4-2 with k_v of 0.568×10^{-6} cm/s in the dry shrinkage tests are 9.63%, 8.66% and 5.96%, respectively. The variation of radial strain on the surface of specimens decreased sequentially with the increase of T_{salt} and $N_{\text{F-T}}$. This indicates that saline inhibits the growth of desiccation cracks and has a more noticeable effect on cracking behaviors than the F-T cycles. This case can be divided into two situations for analysis as follows.

(1) The saline precipitated in the pores of specimens with water evaporation on the condition that T_{salt} does not reach saturation state, when air will enter the pores of specimens. However, less air can enter due to the precipitated salt crystals filling the

specimens' pores. The matric suction cannot exceed the cohesive strength between soil particles and failed to affect their arrangement.

(2) As for specimens with saturated saline, NaCl is simultaneously dissolved in the free water and distributed in pores before W-D and F-T cycles. The saline crystals in pores restrain the migration of water molecules to the specimens' surface for water evaporation leading to its decreasing rate. Saline is crystalized and filled in pores of specimens along with the evaporation of free water [52].

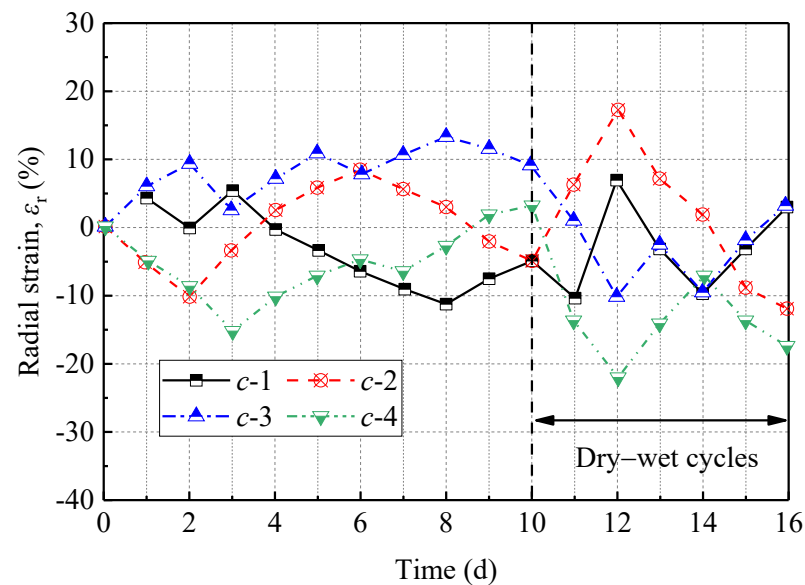


Figure 16. Variation curves of radial strain with time on RC-1.35-4-2 surface.

3.3. Discussion

The common treatment approaches for inhibiting shrinkage and desiccation of red clay comprise the physical method of compaction degree improvement and stabilization techniques by curing agents. Increasing the initial compaction degree can inhibit water loss and shrinkage of red clay. The suction of compacted red clay increases after dewatering and microfracture derivation leads to a decrease in strength due to liquid removal. Lime-meta-kaolin-treated red clay is a novel treatment method to mitigate shrinkage behavior through improving moisture sensitivity, in which amorphous silicon and aluminum with an edge-surface contacted structure in meta-kaolin can capture calcium ions in hydroxide solution and form cementation hydrates between grains or particles of red clay [55]. In addition, the nano-silica particles, as environmentally friendly curing agent, are mixed with red clay to inhibit the shrinkage through filling pores with diameter greater than $0.03\mu\text{m}$. This solidification method can sufficiently alter the physico-mechanical characteristics and is beneficial in restraining the shrinkage cracking of red clay. However, more attention should be given to the behavior and mechanism of red clay subjected to W-D cycles without considering saline intrusion and F-T cycles. Further research on inhibiting shrinkage cracking of red clay upon F-T cycles and saline intrusion should be carried out and related treatment methods need to be proposed.

4. Conclusions

In this study, the effects of F-T cycles and saline intrusion on permeability characteristics and desiccation cracking of Dalian red clay in China were investigated via laboratory tests. The evolution of desiccation cracks of compacted specimens induced by W-D cycles was monitored using a photographing system and quantified by a Digital Image Correlation technique. The following conclusions are drawn from the experimental results:

(1) The permeability coefficient of compacted specimens increases with N_{F-T} under the constant ρ_d and presents an overall increasing trend with the increase of N_{F-T} under

constant T_{salt} . However, the permeability coefficient of specimens with the constant T_{salt} decreases with the increase of ρ_d . The greatest increment of permeability coefficient occurs after the first F-T cycle regardless of specimens with variable T_{salt} and ρ_d .

(2) The quantitative relationship between the number of F-D cycles and the permeability coefficient can be expressed by the exponential function. The evaporation rate of water on the surface of specimens decreases with T_{salt} of specimens. Dry density has the more apparent influence on desiccation cracking than salt concentration and F-T cycle to some extent for red clay.

(3) The increase of dry density has a certain inhibitory effect on the desiccation cracking of specimens under W-D cycles. The F-T cycles have a modest promoting effect on crack propagation on the surface of saturated red clay. Saline inhibits the growth of desiccation cracks and has a more noticeable effect on cracking behaviors than the F-T cycles.

Author Contributions: Conceptualization, C.Z. and X.L.; Methodology, C.C.; Validation, X.P.; Investigation, C.C. and Y.P.; Resources, X.L. and P.J.; Data curation, Y.P.; Writing—original draft, C.Z.; Visualization, C.Z.; Funding acquisition, P.J. All authors have read and agreed to the published version of the manuscript.

Funding: This work is supported by the Natural science foundation for colleges and universities in Jiangsu Province (21KIB560018). The authors also wish to thank Shenyang Jianzhu University for providing the access to the software and other facilities.

Institutional Review Board Statement: Not applicable.

Informed Consent Statement: Not applicable.

Data Availability Statement: All data and models generated or used during the study appear in the submitted article.

Conflicts of Interest: The authors declare no conflict of interest.

References

- Lang, L.; Chen, B.; Chen, B. Strength evolutions of varying water content-dredged sludge stabilized with alkali-activated ground granulated blast-furnace slag. *Constr. Build Mater.* **2021**, *275*, 122111. [\[CrossRef\]](#)
- Zeng, L.; Yu, H.; Gao, Q.; Liu, J.; Liu, Z. Evolution of Tensile Properties of Compacted Red Clay under Wet and Dry Cycles. *Ksce J. Civ. Eng.* **2022**, *26*, 606–618. [\[CrossRef\]](#)
- Ding, L.; Han, Z.; Zou, W.; Wang, X. Characterizing hydro-mechanical behaviours of compacted subgrade soils considering effects of freeze-thaw cycles. *Transp. Geotech.* **2020**, *24*, 100392. [\[CrossRef\]](#)
- Lu, Y.; Liu, S.; Weng, L.; Wang, L.; Li, Z.; Xu, L. Fractal analysis of cracking in a clayey soil under freeze-thaw cycles. *Eng. Geol.* **2016**, *208*, 93–99. [\[CrossRef\]](#)
- Lyu, H.; Gu, J.; Li, W.; Liu, F. Analysis of compressibility and mechanical behavior of red clay considering structural strength. *Arab. J. Geosci.* **2020**, *13*, 411. [\[CrossRef\]](#)
- Zhang, Y.; Johnson, A.E.; White, D.J. Freeze-thaw performance of cement and fly ash stabilized loess. *Transp. Geotech.* **2019**, *21*, 100279. [\[CrossRef\]](#)
- Wu, H.; Jin, F.; Du, Y. Influence of wet-dry cycles on vertical cutoff walls made of reactive magnesia-slag-bentonite-soil mixtures. *J. Zhejiang Univ-Sc a* **2019**, *20*, 948–960. [\[CrossRef\]](#)
- Wu, H.; Du, Y.; Yu, J.; Yang, Y.; Li, V.C. Hydraulic conductivity and self-healing performance of Engineered Cementitious Composites exposed to Acid Mine Drainage. *Sci. Total Environ.* **2020**, *716*, 137095. [\[CrossRef\]](#)
- Lai, F.; Zhang, N.; Liu, S.; Yang, D. A generalised analytical framework for active earth pressure on retaining walls with narrow soil. *Géotechnique* **2022**, 1–46. [\[CrossRef\]](#)
- Lin, J.; Zou, W.; Han, Z.; Zhang, Z.; Wang, X. Structural, volumetric and water retention behaviors of a compacted clay upon saline intrusion and freeze-thaw cycles. *J. Rock Mech. Geotech.* **2022**, *14*, 953–966. [\[CrossRef\]](#)
- Mishra, P.N.; Scheuermann, A.; Bore, T.; Li, L. Salinity effects on soil shrinkage characteristic curves of fine-grained geomaterials. *J. Rock Mech. Geotech.* **2019**, *11*, 181–191. [\[CrossRef\]](#)
- Thyagaraj, T.; Das, A.P. Physico-chemical effects on collapse behaviour of compacted red soil. *Géotechnique* **2017**, *67*, 559–571. [\[CrossRef\]](#)
- Lang, L.; Chen, B. Strength Properties of Cement-Stabilized Dredged Sludge Incorporating Nano-SiO₂ and Straw Fiber. *Int. J. Geomech.* **2021**, *21*, 04021119. [\[CrossRef\]](#)
- Sagidullina, N.; Abdialim, S.; Kim, J.; Satyanaga, A.; Moon, S. Influence of Freeze–Thaw Cycles on Physical and Mechanical Properties of Cement-Treated Silty Sand. *Sustainability* **2022**, *14*, 7000. [\[CrossRef\]](#)

15. Lang, L.; Chen, B.; Li, J. High-efficiency stabilization of dredged sediment using nano-modified and chemical-activated binary cement. *J. Rock. Mech. Geotech.* **2023**. [[CrossRef](#)]
16. Qi, J.; Vermeer, P.A.; Cheng, G. A review of the influence of freeze-thaw cycles on soil geotechnical properties. *Permafr. Periglac.* **2006**, *17*, 245–252. [[CrossRef](#)]
17. Liu, J.; Chang, D.; Yu, Q. Influence of freeze-thaw cycles on mechanical properties of a silty sand. *Eng. Geol.* **2016**, *210*, 23–32. [[CrossRef](#)]
18. Dalla Santa, G.; Cola, S.; Secco, M.; Tateo, F.; Sassi, R.; Galgaro, A. Multiscale analysis of freeze–thaw effects induced by ground heat exchangers on permeability of silty clays. *Géotechnique* **2019**, *69*, 95–105. [[CrossRef](#)]
19. Chamberlain, E.J.; Gow, A.J. Effect of freezing and thawing on the permeability and structure of soils. *Eng. Geol.* **1979**, *13*, 73–92. [[CrossRef](#)]
20. Eigenbrod, K.D. Effects of cyclic freezing and thawing on volume changes and permeabilities of soft fine-grained soils. *Can. Geotech. J.* **1996**, *33*, 529–537. [[CrossRef](#)]
21. Othman, M.A. *Effect of Freeze-Thaw on the Structure and Hydraulic Conductivity of Compacted Clays*; The University of Wisconsin-Madison: Madison, WI, USA, 1992.
22. Benson, C.H.; Othman, M.A. Hydraulic Conductivity of Compacted Clay Frozen and Thawed In Situ. *J. Geotech. Eng.* **1993**, *119*, 276–294. [[CrossRef](#)]
23. Thyagaraj, T.; Thomas, S.R.; Das, A.P. Physico-Chemical Effects on Shrinkage Behavior of Compacted Expansive Clay. *Int. J. Geomech.* **2017**, *17*, 06016013. [[CrossRef](#)]
24. Mokni, N.; Romero, E.; Olivella, S. Chemo-hydro-mechanical behaviour of compacted Boom Clay: Joint effects of osmotic and matric suctions. *Géotechnique* **2014**, *64*, 681–693. [[CrossRef](#)]
25. Rao, S.M.; Thyagaraj, T.; Thomas, H.R. Swelling of compacted clay under osmotic gradients. *Géotechnique* **2006**, *56*, 707–713. [[CrossRef](#)]
26. Palomino, A.M.; Santamarina, J.C. Fabric map for kaolinite: Effects of pH and ionic concentration on behavior. *Clays Clay Miner.* **2005**, *53*, 211–223. [[CrossRef](#)]
27. Zhang, C.; Liu, S.; Zhang, D.; Lai, F.; Lu, T.; Liu, Y. A modified equal-strain solution for consolidation behavior of composite foundation reinforced by precast concrete piles improved with cement-treated soil. *Comput. Geotech.* **2022**, *150*, 104905. [[CrossRef](#)]
28. Barbour, S.L.; Fredlund, D.G. Mechanisms of osmotic flow and volume change in Clay soils. *Can. Geotech. J.* **1989**, *26*, 551–562. [[CrossRef](#)]
29. Wan, Y.; Xue, Q.; Liu, L.; Wang, S. Relationship between the shrinkage crack characteristics and the water content gradient of compacted clay liner in a landfill final cover. *Soils Found* **2018**, *58*, 1435–1445. [[CrossRef](#)]
30. Chong, B. Simulation of crack growth using cohesive crack method. *Ksce J. Civ. Eng.* **2010**, *14*, 765–772. [[CrossRef](#)]
31. Tang, C.; Cheng, Q.; Leng, T.; Shi, B.; Zeng, H.; Inyang, H.I. Effects of wetting-drying cycles and desiccation cracks on mechanical behavior of an unsaturated soil. *Catena* **2020**, *194*, 104721. [[CrossRef](#)]
32. Ye, W.M.; Wan, M.; Chen, B.; Chen, Y.G.; Cui, Y.J.; Wang, J. An unsaturated hydraulic conductivity model for compacted GMZ01 bentonite with consideration of temperature. *Environ. Earth Sci.* **2014**, *71*, 1937–1944. [[CrossRef](#)]
33. Li, J.H.; Lu, Z.; Guo, L.B.; Zhang, L.M. Experimental study on soil-water characteristic curve for silty clay with desiccation cracks. *Eng. Geol.* **2017**, *218*, 70–76. [[CrossRef](#)]
34. Li, J.H.; Zhang, L.M. Study of desiccation crack initiation and development at ground surface. *Eng. Geol.* **2011**, *123*, 347–358. [[CrossRef](#)]
35. Lakshmikantha, M.R.; Prat, P.C.; Ledesma, A. Experimental evidence of size effect in soil cracking. *Can Geotech. J.* **2012**, *49*, 264–284. [[CrossRef](#)]
36. Costa, S.; Kodikara, J.; Barbour, S.L.; Fredlund, D.G. Theoretical analysis of desiccation crack spacing of a thin, long soil layer. *Acta Geotech.* **2018**, *13*, 39–49. [[CrossRef](#)]
37. Pouya, A.; Vo, T.D.; Hemmati, S.; Tang, A.M. Modeling soil desiccation cracking by analytical and numerical approaches. *Int. J. Numer Anal Met.* **2019**, *43*, 738–763. [[CrossRef](#)]
38. Tang, C.; Cui, Y.; Shi, B.; Tang, A.; Liu, C. Desiccation and cracking behaviour of clay layer from slurry state under wetting–drying cycles. *Geoderma* **2011**, *166*, 111–118. [[CrossRef](#)]
39. Tang, C.; Pei, X.; Wang, D.; Shi, B.; Li, J. Tensile Strength of Compacted Clayey Soil. *J. Geotech. Geoenviron.* **2015**, *141*, 04014122. [[CrossRef](#)]
40. *ASTM D2487-11*; Standard Practice for Classification of Soils for Engineering Purpose (Unified Soil Classification System). ASTM International: West Conshohocken, PE, USA, 2011.
41. *ASTM D854-10, 2010*; Standard Methods for Specific Gravity of Soils by Water Pycnometer. ASTM International: West Conshohocken, PE, USA, 2010.
42. *ASTM D560*; Standard Test Methods for Freezing and Thawing Compacted Soil-Cement Mixtures. ASTM International: West Conshohocken, PE, USA, 2016.
43. Cai, G.H.; Liu, S.Y.; Zheng, X. Effects of Drying-Wetting Cycles on Durability of Carbonated Reactive Magnesia-Admixed Clayey Soil. *J. Mater. Civil. Eng.* **2019**, *31*, 4019276. [[CrossRef](#)]
44. Cai, G.; Liu, S.; Zheng, X. Influence of drying-wetting cycles on engineering properties of carbonated silt admixed with reactive MgO. *Constr. Build Mater.* **2019**, *204*, 84–93. [[CrossRef](#)]

45. GB/T 50123-2019; Standard for Geotechnical Testing Method. 2019.
46. Li, H.; Tan, Y.; Xie, Z.; Sun, D.; Sun, W. Method for measuring the saturated permeability coefficient of compacted bentonite at temperatures exceeding 100 °C. *Prog. Nucl. Energ.* **2021**, *141*, 103958. [[CrossRef](#)]
47. Tang, C.; Shi, B.; Liu, C.; Zhao, L.; Wang, B. Influencing factors of geometrical structure of surface shrinkage cracks in clayey soils. *Eng. Geol.* **2008**, *101*, 204–217. [[CrossRef](#)]
48. Tran, D.K.; Ralaizafisoarivony, N.; Charlier, R.; Mercatoris, B.; Léonard, A.; Toye, D.; Degré, A. Studying the effect of desiccation cracking on the evaporation process of a Luvisol—From a small-scale experimental and numerical approach. *Soil Tillage Res.* **2019**, *193*, 142–152. [[CrossRef](#)]
49. Liu, C.; Tang, C.; Shi, B.; Suo, W. Automatic quantification of crack patterns by image processing. *Comput. Geosci.-Uk* **2013**, *57*, 77–80. [[CrossRef](#)]
50. Ying, Z.; Cui, Y.; Benahmed, N.; Duc, M. Salinity effect on the compaction behaviour, matric suction, stiffness and microstructure of a silty soil. *J. Rock Mech. Geotech.* **2021**, *13*, 855–863. [[CrossRef](#)]
51. Ying, Z.; Benahmed, N.; Cui, Y.; Duc, M. Determining osmotic suction through electrical conductivity for unsaturated low-plasticity soils. *J. Rock Mech Geotech.* **2022**, *6*, 1946–1955. [[CrossRef](#)]
52. Newson, T.A.; Fahey, M. The effect of soil suction on evaporative fluxes from soil surfaces: Discussion. *Can. Geotech. J.* **1998**, *35*, 692–694. [[CrossRef](#)]
53. Young, R. *Soil Properties and Behaviour*; Elsevier: Amsterdam, The Netherlands, 2012; Volume 5.
54. Ying, Z.; Cui, Y.; Benahmed, N.; Duc, M. Drying effect on the microstructure of compacted salted silt. *Géotechnique* **2021**, *73*, 62–70. [[CrossRef](#)]
55. Tan, Y.; Hu, Y.; Deng, Y.; Cao, L.; Zuo, Q.; Ming, H. Behavior and mechanism of laterite shrinkage inhibition with lime and meta-kaolin mixture. *Rock Soil Mech.* **2019**, *40*, 4213–4219.

Disclaimer/Publisher’s Note: The statements, opinions and data contained in all publications are solely those of the individual author(s) and contributor(s) and not of MDPI and/or the editor(s). MDPI and/or the editor(s) disclaim responsibility for any injury to people or property resulting from any ideas, methods, instructions or products referred to in the content.